SPH simulations of thixo-viscoplastic fluid flow past a cylinder

E. Rossi[a,*], I. Garcia de Beristain[a], A. Vazquez-Quesada[b], J. E. López-Aguilar[c], M. Ellero[a,d,e]

[a]*BCAM - Basque Center for Applied Mathematics, Alameda Mazarredo 14, 48009, Bilbao, Spain*
[b]*Departamento de Física Fundamental, UNED, Apartado 60141, 28080 Madrid, Spain.*
[c]*Facultad de Química, Departamento de Ingeniería Química, Universidad Nacional Autónoma de México (UNAM), Ciudad Universitaria, Coyoacán, CDMX 04510, Mexico*
[d]*IKERBASQUE, Basque Foundation for Science, Calle de María Díaz de Haro 3, 48013 Bilbao, Spain*
[e]*Zienkiewicz Centre for Computational Engineering (ZCCE), Swansea University, Swansea SA1 8EN, UK*

Abstract

Thixotropic materials are complex fluids that display time-dependent viscosity and/or yield-stress response upon the application of a fixed deformation, while recovering their original structured-state when the deformation is discontinued. Thixotropic effects are presents in many different systems and applications, ranging from food products, such as in ketchup, to metals, such as molten aluminium. In this work we present a first attempt to simulate the rheological properties of thixo-viscoplastic flows using a Smoothed Particle Hydrodynamic (SPH) method. A 2D flow around a circular cylinder set up is used in this study, alongside a simple shear flow between parallel plates to validate our numerical predictions. SPH solutions are compared with independent results using the open-source Finite Volume Method solver RheoTool, based in OpenFOAM. The viscoplastic model used in this work is the Papanastasiou model. In order to include thixotropy in the viscoplastic picture, a hybrid constitutive equation is proposed, in which the Papanastasiou model is combined with a microstructural

---
*Corresponding author

Email addresses: `erossi@bcamath.org` (E. Rossi), `igarcia@bcamath.org` (I. Garcia de Beristain), `a.vazquez-quesada@fisfun.uned.es` (A. Vazquez-Quesada), `jelopezaguilar@quimica.unam.mx` (J. E. López-Aguilar), `mellero@bcamath.org` (M. Ellero)

one proposed recently by Le-Cao et al. Phys. Fluids 32 (2020) 123106. Under such thixo-viscoplastic framework, we analyse the flow properties in terms of yield-fronts, streamlines and structure-parameter fields at different Bingham and Thixotropy numbers, through microstructural thixotropic and yield-stress parameter variation. Here, our main findings come in the form of an asymmetry about the cylinder, attributed to the thixo-viscoplastic features of the hybrid model.

Key words: Viscoplasticity, Thixotropy, SPH

1. Introduction

Thixotropy is one of the long-standing and more complex rheological phenomena found in nature [1–4]. Following the recent definition provided by Wei and Larson [4], ideal thixotropy is defined as a reversible and continuous slow
5   time-dependent decrease of viscosity and/or yield-stress when a sample is subjected to a constant shear-rate that induces structural changes in the material [3–10]. This dissipative response reflects in the development of a thixotropic time-scale which originates from the time required for the microstructure to change upon flow [3]. An ideal thixotropic fluid may require a long time to
10   reach a steady-state in a start-up flow but relaxes quickly or even nearly instantaneously upon flow cessation [4]. Usual rheological phenomena associated with thixotropy are shear-thinning, stress overshoots in start-up flow and hysteresis [3]. Different materials displaying thixotropy cover a wide range in type and variety, and are exploited in technological applications, such as colloidal
15   suspensions and gels, emulsions, polymer, paints, foams, minerals, oils, drilling muds, food products, detergents, slurries, biofluids, cosmetics, pharmaceuticals, biomedical materials, ceramics, soils, metals, inks, concrete, among other [3, 4, 10, 11].

There are two main constitutive modelling paradigms for thixotropic materi-
20   als: (i) phenomenological continuum-mechanics models and (ii) microstructural models [2, 3, 12]. The phenomenological models are based on stress equations,

which may or may not include viscoelasticity, connected to variables, such as a structure-parameter [13], viscosity or fluidity [14], which indirectly measure the material internal structure. The microstructural models aim to quantify the grade of structuring of the material from more complicated chemical-kinetics-like equations measuring the dynamics of formation and breakage of bonds in the material. In this work, we will assume the phenomenological approach with a model considering thixotropic and viscoplastic responses via a regularised Papanastasiou model for viscoplasticity and a structure-parameter based equation for thixotropy. This model follows the ideas proposed by Le-Cao et al. [15].

Numerical solutions of complex thixo-viscoplastic flow has been tackled in the past with different algorithms and constitutive modelling approaches. Syrakos et al. [16] studied the flow past a smooth cylinder with finite-elements, mixing inertial and thixotropic features using a variant of the Moore constitutive model. These authors found thixotropic parameters influential in the flow-structure (vortex enclosing unyielded patches behind the cylinder without shedding even when inertia was present) and drag coefficients. In a setting given under a Bingham-Papanastasiou constitutive model, Mahmood et al. [17] simulated the flow of a viscoplastic fluid past a cylinder at $Re = 20$ using a mixed finite element formulation; this formulation reflects the main features of time-independent yield-stress materials with symmetrical flow-fields and larger unyielded regions as well as drag-coefficients with increasing Bingham numbers. Bui and Ho [18–20] used Papanastasiou-regularised Bingham and Herschel-Bulkley model variants alongside a thixo-viscoplastic Moore model. With these and using the ANSYS commercial software, asymmetrical yield-fronts were reported under inertial $Re = 20$ and viscoplastic $Bn = 0.2$ conditions. Different vortex-phases resulted, ranging from vortex absence, passing through elongated vortices in the cylinder wake that enclose solid-like patches, to transient vortex-shedding at high Reynolds numbers; these kinematic structures decline with plasticity.

Some of the earliest applications of Smoothed Particle Hydrodynamics (SPH) to simulate non-Newtonian fluids date back to early 2000s [21, 22] where different types of viscoelastic models where simulated. Since then, it has been

successfully used to model different kinds of non-Newtonian fluids including viscoplasticity. In particular, the range of applications of the SPH model to the simulation of viscoplastic flows goes from debris, sediment and granular flows (see e.g. [23], [24], [25], [26], [27] or [28]), to multiphase flows (see e.g. [29], [30] or [31]) and to fluid/structures interactions (see e.g. [32] or [33]).

Despite the large number of applications, SPH models have been used for validation of the viscoplastic fluids, in terms of Poiseuille or Couette flows only (see e.g. [34], [35], [26] and [28]), or in comparisons with experimental results (see e.g. [23], [29] and [26]). However, rigorous complex flow validations, such as the ones in [36] and [37], in terms of yielded and un-yielded regions for the 2D viscoplastic flow around a cylinder, can not be found in literature.

In addition, the use of SPH to model thixotropic fluids can be found only in few studies: one related to free surface flow in dam-break applications [38] and the other related to the interfacial-flows in the ascent of bubbles in thixotropic materials e.g. [39].

The aim of this study is to accurately analyse the 2D thixo-viscoplastic fluid flow around a cylinder using a Smoothed Particles Hydrodynamics (SPH) method. The paper is divided into four main sections. In Sec. 2 the SPH model is discussed, together with details about the fluid (Sec. 2.1) and the solid boundary conditions (Sec. 2.2). In Sec. 3 the viscoplastic Bingham model and the Papanastasiou regularization are presented, together with their validation (Sec. 3.1) on both simple shear (Sec. 3.1.1) and flow around a cylinder (Sec. 3.1.2) cases. In Sec. 4, the thixotropic model used is described: Sec. 4.1 contains the model validation using simple shear cases, while Sec. 4.2 the results obtained analysing the flow around the cylinder. In Sec. 5 a brief and comprehensive overview of the study and conclusions are given.

2. The SPH model

In this section, the SPH method used in this work is presented. The method description is divided in different subsections, as follows: in Sec. 2.1, details of

4

the solvent medium are given, while in Sec. 2.2, the solid boundary conditions are described.

2.1. Suspending fluid

The SPH method is a mesh-less Lagrangian model, in which the momentum equations describing the motion of the suspending fluid are discretized by a set of N_{SPH} points termed *fluid particles*. Positions and momenta of every fluid particle evolve according to the following equations (obtained modifying the original model presented in [40] for fluids with non-constant viscosities):

$$
\begin{cases}
\dot{\boldsymbol{r}}_i = \boldsymbol{v}_i, \\
\\
m\dot{\boldsymbol{v}}_i = -\sum_j \left[\dfrac{P_i}{d_i^2} + \dfrac{P_j}{d_j^2} \right] \dfrac{\partial W(r_{ij})}{\partial r_{ij}} \boldsymbol{e}_{ij} + \\
\\
\quad\quad + \sum_j \left(\dfrac{D}{3} + 9 \right) \left(\dfrac{\eta_i + \eta_j}{2} \right) \dfrac{\partial W(r_{ij})}{\partial r_{ij}} \dfrac{\boldsymbol{e}_{ij} \cdot \boldsymbol{v}_{ij}}{d_i d_j r_{ij}} \boldsymbol{e}_{ij},
\end{cases}
\tag{1}
$$

85   where m is the fluid particle mass, $i = 1, .., N_{SPH}$ is the fluid particle index, P_i the pressure of particle i, $\boldsymbol{e}_{ij} = \boldsymbol{r}_{ij}/r_{ij}$ the unit vector joining particles i and j, η_i is the viscosity of particle i and $\boldsymbol{v}_{ij} = \boldsymbol{v}_i - \boldsymbol{v}_j$ their velocity difference. $d_i = \sum_j W(r_{ij}, r_{cut})$ is the number density of particle i estimated as a weighted interpolation with kernel function W with compact support r_{cut} [40], while D

90   is the number of dimensions of the system. Using this definition, continuity equation for the mass density $\rho_i = md_i$ is automatically satisfied.

If the fluid is Newtonian, $\eta_j = const.$ for each SPH particle $j = 1, ..., N_{SPH}$; in the case of a non-Newtonian fluid, the viscosity is allowed to vary on each SPH particle depending on the specific constitutive model used. Two different

95   non-Newtonian fluid models are studied in this work: a Papanastasiou model for viscoplastic fluids, that is described in Sec. 3, and a thixo-viscoplastic model that is described in Sec. 4.

The Newton's equations of motion Eq. (1) are a discrete representation of the momentum Navier-Stokes equation in a Lagrangian framework: the first

summation in Eq. (1) determines the pressure gradient term, while the second specifies the viscous forces. A quintic spline kernel [41] with cut-off radius $r_{cut} = 4\,\Delta r$ is used for the weighting function W [42], where Δr is the mean fluid particle separation. Finally, the following equation-of-state is used for the pressure:

$$P_i = p_0 \left[\left(\frac{\rho_i}{\rho_{ref}} \right)^\gamma - 1 \right], \tag{2}$$

where $\rho_{ref} = 0.99\rho_0$ ensures a positive pressure field and the input parameters ρ_0, p_0 and γ are chosen to have a speed of sound $c_s = \sqrt{\gamma p_0/\rho_0}$ larger than any other velocity present in the problem, therefore enforcing approximate incompressibility [43].

2.2. Solid boundary conditions

Solid walls of arbitrary shape can be modelled using boundary particles similar to fluid ones as follows [44]. For each solid region and in order to impose the no-slip boundary conditions, several layers of boundary particles are generated inside it using an ad-hoc algorithm. Boundary particles, located inside the solid region, interact with fluid particles through the same SPH forces as described in Eq. (1). To impose the no-slip boundary conditions, the velocity of boundary particles should be prescribed. In this work, we follow the approach used in [44], i.e. solid particles are considered neutrally buoyant with density equal to the equilibrium solvent density and the velocities of boundary particles are evaluated using the approach in [41].

To evaluate the boundary-particle velocity let us consider the situation with a fluid particle f near a solid boundary. In this case, the algorithm first calculate the nearest solid surface point s to the fluid particle f in order to define the tangent plane in s. Afterwards, the algorithm assign the following velocities to the boundary particles:

$$\mathbf{v}_b = - \left(\frac{d_b}{d_f} \right) (\mathbf{v}_f - \mathbf{v}_s) + \mathbf{v}_s, \tag{3}$$

where d_b is the normal distance of the boundary particle from the tangent plane, d_f is the distance of the fluid particle from the surface point s and $\mathbf{v}_f$ is the

fluid particle velocity. $\mathbf{v}_s$ is the velocity of the surface point s of the boundary region.

3. The Bingham model and the Papanastasiou regularization

Viscoplastic fluids combine solid-like and fluid-like features (see e.g. [5, 6, 9, 45]). Many of these materials can be described introducing a yield stress τ_y, that is, a critical stress value below which no flow occurs. Then, at stresses smaller than τ_y, these materials appear with absence of flow behaving as a rigid body, while they exhibit a fluid-like response at higher stresses. Various models have been introduced to describe this kind of materials such as the Bingham [46], Herschel-Bulkley [47] or the Casson [48] models but they all present a discontinuity when the shear stress equals the yield stress. In order to avoid this discontinuity various kinds of regularization have been presented such as the Bercovier and Engelman [49] or the Glowinski [50] (for a complete presentation of the viscoplastic model and their regularization the reader may refer to[9]). In this paper we adopt the Papanastasiou regularization [51] applied to the Bingham model:

$$\begin{cases} \eta = \eta_\infty + \dfrac{\tau_y}{\dot{\gamma}}\left(1 - e^{-m\dot{\gamma}}\right), \\ \boldsymbol{\tau} = \left[\eta_\infty + \dfrac{\tau_y}{\dot{\gamma}}\left(1 - e^{-m\dot{\gamma}}\right)\right]\dot{\boldsymbol{\gamma}}, \end{cases} \tag{4}$$

where $\boldsymbol{\tau}$ is the stress tensor, $\dot{\boldsymbol{\gamma}}$ is the strain-rate tensor defined as:

$$\dot{\boldsymbol{\gamma}} = (\nabla\mathbf{v}) + (\nabla\mathbf{v}^T), \tag{5}$$

η is the shear viscosity coefficient and η_∞ is the limiting viscosity attained at large shear-rates. m is is the Papanastasiou exponential regularization parameter, which controls the stress exponential growth. The strain-rate tensor second invariant $\dot{\gamma}$ can be evaluated as:

$$\dot{\gamma} = \sqrt{\frac{1}{2}\Pi_{\dot{\gamma}}} = \left[\frac{1}{2}\{\dot{\boldsymbol{\gamma}} : \dot{\boldsymbol{\gamma}}\}\right]^{1/2}, \tag{6}$$

while the strain-rate tensor second invariants τ is given by:

$$\tau = \sqrt{\frac{1}{2}\Pi_{\boldsymbol{\tau}}} = \left[\frac{1}{2}\{\boldsymbol{\tau} : \boldsymbol{\tau}\}\right]^{1/2} = \eta_\infty\dot{\gamma} + \tau_y\left(1 - e^{-m\dot{\gamma}}\right). \tag{7}$$

It is now possible to define a criterion to track yielded/un-yielded regions based on the stress, i.e. the viscoplastic material will flow only when the magnitude of the stress tensor τ is larger then the yield stress τ_y:

$$\begin{cases} yielded: & \tau > \tau_y, \\ un-yielded: & \tau \leq \tau_y. \end{cases} \tag{8}$$

The Bingham model with the Papanastasiou regularization does not take into account the elasticity or any temporal relaxation and it is based on the following assumptions: the fluid material structure is isotropic and the trace of the stress tensor is always equal to zero. Moreover, the adopted yielding criterion in Eq. (8) is based on a single invariant, the stress tensor second invariant, and corresponds to the von Mises yielding criterion [52] (see e.g. [53]).

Fig. 1 shows the comparison (in terms of shear-stress modulus and viscosity) between the Bingham model and the Papanastasiou regularization for different values of m. It is interesting to note that the Papanastasiou regularization,
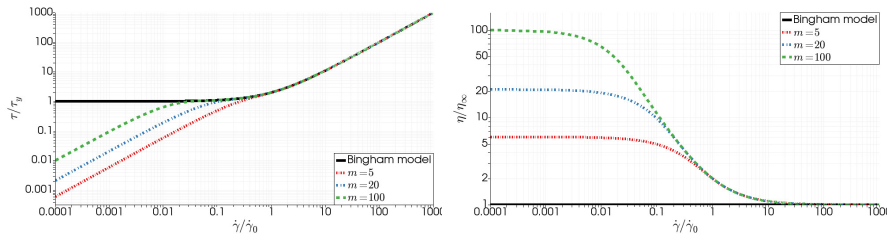
Figure 1: Left: non-dimensional shear stress and Right: non-dimensional viscosity as functions of the non-dimensional shear rate for different values of m. Continuous lines represents the Bingham model. Dotted lines represent the Papanastasiou regularization.

while eliminating the singularity present in the Bingham model, modifies also the τ and η values in the limit of low shear rates, in particular introducing a finite viscosity in the limit $\dot{\gamma} \to 0$, thus providing an apparent yield-stress response in the plastic features [5, 8]:

$$\begin{cases} \dot{\gamma} \to 0: & \eta = \eta_\infty + m\tau_y, \quad \tau = 0, \\ \dot{\gamma} \to \infty: & \eta = \eta_\infty, \qquad\quad \tau = \eta_\infty \dot{\gamma}. \end{cases} \tag{9}$$

8

In the context of the SPH method presented in this paper, the expressions in Eq. (5) for the strain-rate tensor, in (6) for the stress and strain-rate tensors second invariants, as well as Eq. (4) for η and $\boldsymbol{\tau}$, are used to evaluate these quantities for each SPH particle.

It is important to note that for each SPH particle the velocity gradient tensor appearing in Eq. (5) will be evaluated using the following expression:

$$(\nabla \mathbf{v})_i^{\mu\nu} = \sum_j \frac{(\mathbf{v}_i^\mu - \mathbf{v}_j^\mu)(\mathbf{r}_j^\nu - \mathbf{r}_i^\nu)}{d_j r_{ij}} \left. \frac{\partial W(r)}{\partial r} \right|_{r=r_{ij}}, \qquad (10)$$

where i, j are the SPH particle indices, μ and ν are the column and row indexes respectively $\mu, \nu = 1, ..., D$, where D is the number of dimensions of the system, r_{ij} is the modulus of the vector joining particles i and j, d_j is the number density of particle j and $\left. \frac{\partial W(r)}{\partial r} \right|_{r=r_{ij}}$ is the corresponding gradient of the kernel function.

It is interesting to highlight that the SPH time-step, following [41] and [44], is given by:

$$\Delta t = 0.125 \left(\frac{r_{cut}}{3} \right)^2 \frac{\rho_f}{\eta}, \qquad (11)$$

that is, the time-step is inversely proportional to the fluid viscosity. Hence, particular attention must be paid to the choice of the time-step when using the Papanastasiou model. In this case, as shown by Eq. (4), the viscosity depends on the model parameter and attains its maximum value for low shear-rates. As shown in (9) for fixed η_∞ and τ_y, the time-step reduces for increasing m. Correspondingly, m should be chosen sufficiently large in order for the Papanastasiou model to be close enough to the Bingham model but not unnecessarily large in order to avoid too small time-steps. In some situations, the presence of a true yield-stress is also arguable, making viscous models of this type more realistic [5, 8].

3.1. Model validation

The viscoplastic Papanastasiou model has been tested on selected 2D test cases. The obtained results have been compared to theoretical solutions, when

available, and to the results obtained through an alternative Finite Volume Method (FVM) solver: the OpenFoam set of subroutines for rheological simulations Rheotool. OpenFOAM is an open-source finite-volume library able to handle general dynamic unstructured polyhedral meshes, multiphase and multiphysics problems. Two viscoelastic solvers are readily available in OpenFOAM. *viscoelasticFluidFoam* was developed by [54] and has been the ground for many works [55–58]. Additional non-released developments have been published aiming at multiphase problems [59, 60], and improved stabilization mechanisms [57, 61].

In order to make advanced viscoelastic numerical methods available to the OpenFOAM comunity, Pimenta et al. developed *RheoTool* [62] and made it publicly available. RheoTool includes many simulation capabilities, including molecular simulations, electrically driven flows or multiphase simulations. It covers a plethora of constitutive equations and has many numerical stabilization capabilities such as log-conformation methods [63], convective high-resolution schemes, and different pressure-velocity-stress coupling mechanisms.

3.1.1. Simple shear

Three sets of SPH simulations have been performed to test the rheology of the Papanastasiou model using the following values for the regularization parameter $m = \{10, 20, 50\}$. The fluid domain is a square box of size $L = 10$ and, in order to impose a uniform shear flow $\dot{\gamma}$, two rigid plates are considered in the planes normal to the y-direction, moving in opposite directions along the x-axis. Periodic boundary conditions have been set in the x-direction. For all the solutions presented in this section, the SPH resolution used is $L/\Delta r = 50$, where Δr is the mean particle spacing. The total number of SPH particles in this case is $N_{SPH} = 2500$. The fluid viscosity, density and yield stress are $\eta_\infty = 15$, $\rho = 1.0$ and $\tau_y = 10.0$, respectively. The overall fluid viscosity and shear-stress is measured directly from the time-averaged tangential force acting on the walls, i.e.:

$$\eta(\dot{\gamma}) = \frac{F_x}{A\dot{\gamma}}; \quad \tau = \frac{F_x}{A}, \tag{12}$$

where A is the surface of the plates. The obtained results are shown in Fig. 2, where their comparison against the second invariants computed from Eq. (4) shows good agreement.
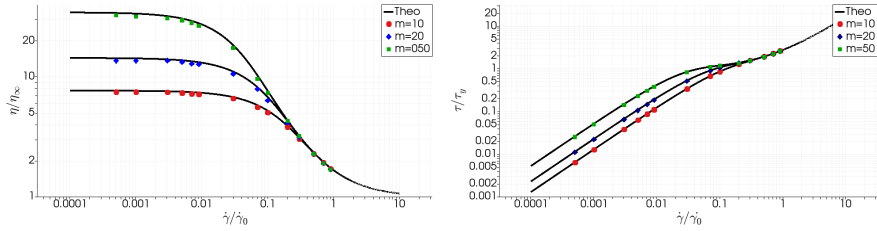

Figure 2: Mean viscosity (left) and shear stress (right) as a function $\dot{\gamma}$. Simulations were performed using three different values of m and fixing $\eta_\infty = 15.0$, $\rho = 1.0$ and $\tau_y = 10.0$. Results are compared with the theoretical value given by Eq. (4). The shear-rate has been made non-dimensional using $\dot{\gamma}_0 = 1$ as a characteristic shear-rate.

165

3.1.2. 2D flow around a cylinder

Computational setup

To simulate the flow around a cylinder we use the following setup as described in Fig. 3: two rigid plates are considered on the top and bottom boundaries moving in the x direction with constant velocity $U_0 = 1$. Periodic boundary conditions have been set on the left and right boundaries where velocity is free to be calculated and transmitted by periodicity.

170
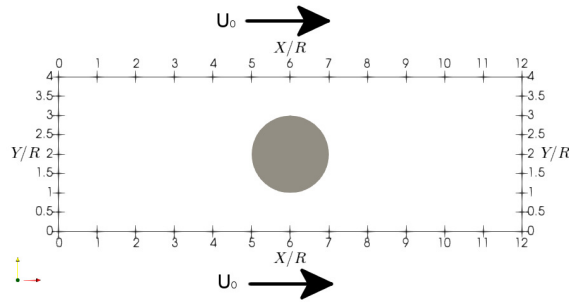
Figure 3: Computational setup for the 2D simulations of the flow around a cylinder.

11

In all the following simulations the cylinder radius is $R = 1$, the cylinder and fluid densities are both equal $\rho_c = \rho_f = 1$, fluid viscosity for high shear-rate is $\eta_\infty = 15$, the speed of sound is $c_{sound} = 150$, the number of SPH particles on the cylinder radius is $N_R = R/\Delta r = 20$ and we use 4 SPH particles on the SPH cut-off radius, $r_{cut}/\Delta r = 4$. This choice of parameters was shown to lead to convergence results in [42]. Following the analysis reported in [36] the parameter $m = 10$ has been chosen here.

Simulations results

To correctly analyse and study the flow around an infinite cylinder immersed in a viscoplastic fluid, the Reynolds number is no longer sufficient to describe the physics of the problem but there is the need to introduce another non-dimensional quantity, i.e. the Bingam number Bn which is defined as the ratio of yield stress to a characteristic viscous stress (in this case referred to that found under η_∞) in the following way:

$$Bn = \frac{2\tau_y R}{\eta_\infty U_0}. \tag{13}$$

Bn close to zero means that the viscous stresses are much larger the the yield stress, for which a viscous response dominates. On opposite, $Bn >> 1$ means that τ_y is much larger than the viscous stresses and the fluid displays a viscoplastic solid-like response.

Simulations have been performed using three different Bingham numbers $Bn = \{0.1, 1.0, 10.0\}$ and the corresponding SPH solutions are compared against those obtained with the FVM-based Rheotool software. In particular we compare, for the same problem setup, the yielded (depicted in white) and un-yielded (depicted in black) regions attained at steady-state using the yielding criterion given by Eq. (8). In order to remove small fluctuations from the plotted fields, the yield-fronts shown here for the SPH simulations are obtained averaging over at least ten time steps after reaching the steady-state.

A first set of simulations have been performed using $L_x = 12R$ and $L_y = 4R$. In this case, the total number of SPH particles is $N_{SPH} = 19200$ and an example of the initial particle distribution can be seen in left plot of Fig. 4.

The mesh used for the FVM simulations has been generated using the Open-FOAM utility blockMesh meshing a quarter of the total geometry and then mirroring on the x-direction. An example of the mesh used for the FVM simulations can be seen in right plot of Fig. 4. Three different domains where used to generate the whole mesh: one domain is used to discretize the pipe (blue region in the right plot of Fig. 4) and two domains are used to generate the grid around the quarter sphere (green and red regions in right right plot of Fig. 4). For the $L_x = 24$ domain, the pipe region is subdivided into 120 cells in the x-direction and 70 cells in the y-direction with a vertical first to last expansion ratio of 3. The regions around the quarter sphere are subdivided in 70 cells in angular direction with an expansion ratio of 3 (to be conformal with the pipe region). Same geometrical values where kept for the $L_x = 12$ domain, but a subdivision of 50 cells were used in the x-direction to account for the shorter geometry.
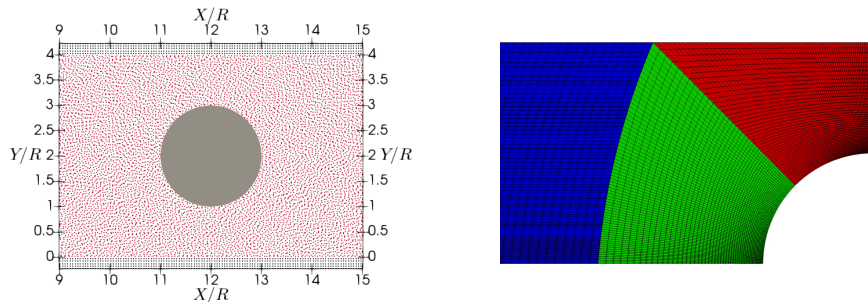
Figure 4: Left: close-up view of the initial SPH particles distribution around the cylinder. Fluid particles are displayed in red why the walls in black. Right: close-up view around the cylinder of the Rheotool mesh.

In Fig. 5, SPH versus FVM yield-fronts are compared for L_x=12. A fairly good agreement is obtained for the two numerical algorithms. Bn-increase brings about the growth of unyielded regions at the geometry centre-line and the rising of triangular unyielded patches with base on the upper and lower walls, accompanied by relatively smaller semicircular on the cylinder equator. As expected, fore-aft symmetry is retained with Bn-rise in these viscoplastic

solutions.

In Fig. 6, a second set of steady-state solutions are illustrated for the yield-fronts using the same Bingham numbers as in Fig. 5, but changing the domain length in the x-direction to $L_x = 24$. In this case the number of SPH particles used is $N_{SPH} = 38400$. It is interesting to note that for $Bn \geq 1.0$, small un-yielded islands are present over the cylinder poles. These un-yielded islands grow in size with Bn-increase, accompanied by triangular un-yielded regions on the top and bottom walls upstream and downstream of the islands, and relatively diminished semicircular patches on the equator in both sides of the cylinder.

A convergence study is performed next. This study is important to see whether it is possible to reduce the resolution while still being able to accurately capture all the flow features. The flow around an infinite cylinder is simulated using $L_x = 24$ and varying the number of points on the cylinder radius $N_R = \{5, 10, 20\}$, corresponding to a total numer of SPH particles of $N_{SPH} = \{2400, 9600, 38400\}$. Yielded and un-yielded regions obtained at steady-state for the three different resolutions and the two Bingham number used are shown in Fig. 7. The general shape of the yielded regions are well reproduced in all three simulations. However, only the simulations with $N_R = 20$ are able to capture quantitatively the small un-yielded islands in the poles of the cylinder.

In Fig. 8, the yielded regions together with the local viscosity for the flow around a cylinder with $L_x = 24$ are reported. The local viscosity has been evaluated using Eq. (4). In this case it is interesting to note that the un-yielded regions (black regions in the left plots of Fig. 8) correspond in size and location to the regions of higher viscosity (colored in red in the right plots of Fig. 8).

Finally, a last set of simulations has been performed at $Bn = 10.0$ while varying $m = 10, 20, 50$ to check the effect of the regularization parameter on the yielded regions. As shown in Fig. 9 the yielded regions are very similar for all the three regularization parameters used while the viscosity inside the un-yielded regions increases for increasing m as expected from Eq. (4). This means

14

that using $m = 10$ is a good compromise between low computational time and physical accuracy: as shown by Eq. (11) the computational time step decreases with increasing viscosity while the viscosity increases for increasing m, as shown by Eq. (4).
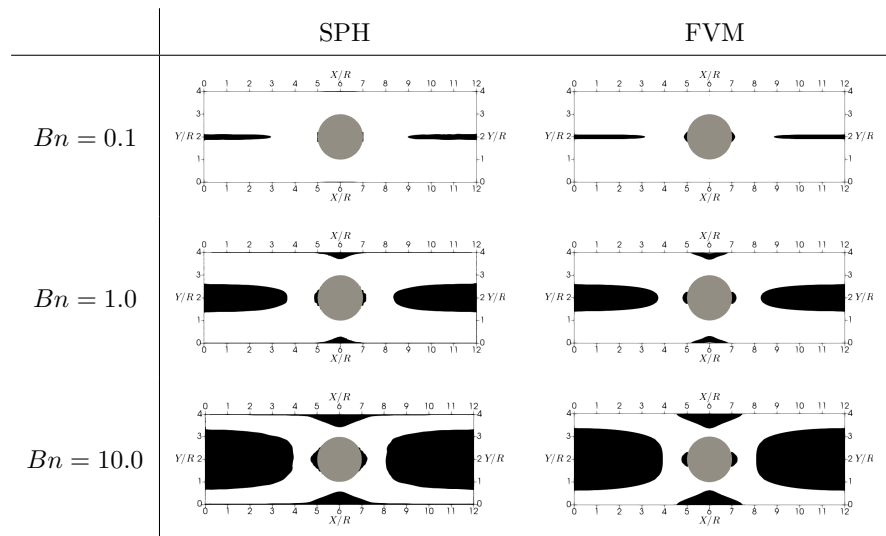

Figure 5: Viscoplastic SPH model; comparison between SPH (left) and FVM (right) simulations for the case $L_x = 12$. From top to bottom: $Bn = \{0.1, 1.0, 10.0\}$.
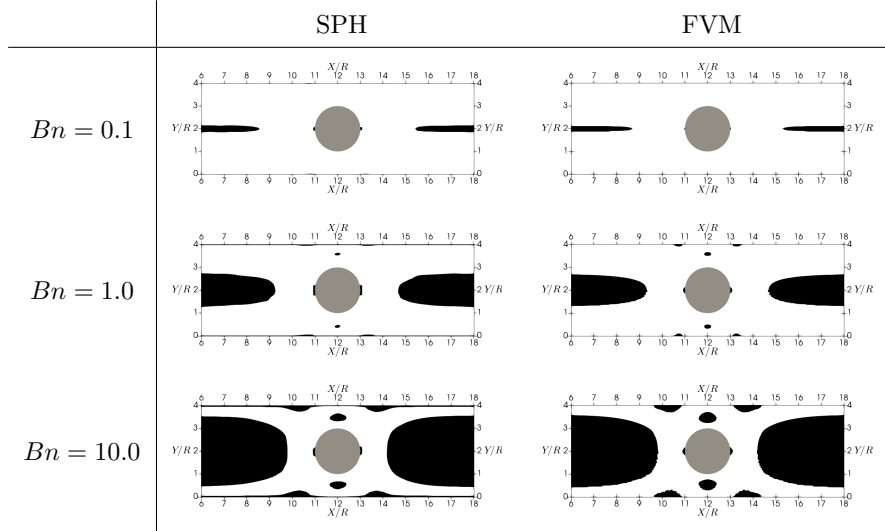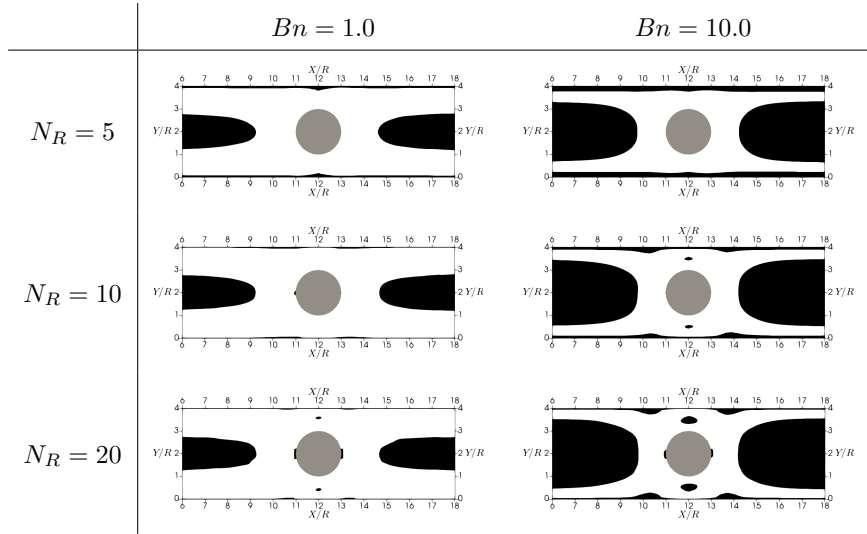
Figure 6: ᵒtextcolorblueViscoplastic SPH model; comparison between SPH (left) and FVM (right) simulations for the case $L_x = 24$. From top to bottom: $Bn = \{0.1, 1.0, 10.0\}$.

Figure 7: Viscoplastic SPH model for the flow around an infinite cylinder using three different resolutions. From top to bottom $N_R = \{5, 10, 20\}$. Left column $Bn = 1.0$. Right column $Bn = 10.0$.
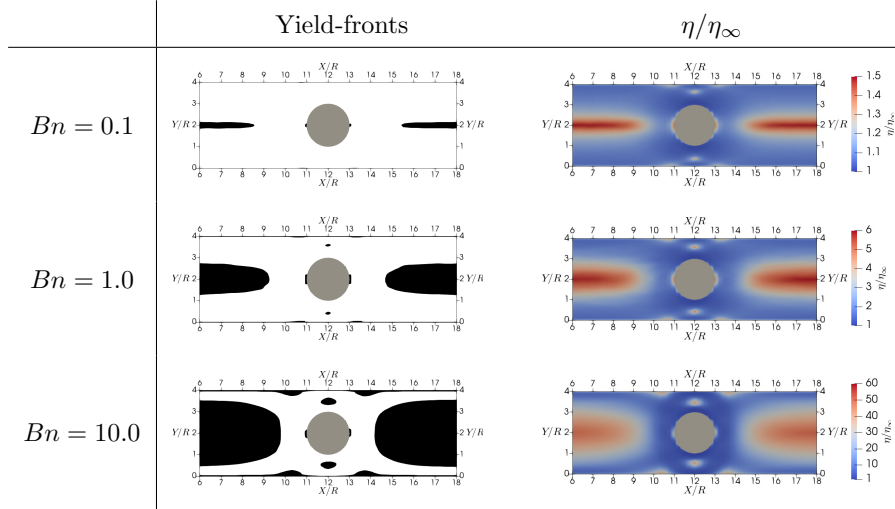
Figure 8: Viscoplastic SPH model for the 2D flow around a cylinder with $L_x = 24$. From top to bottom $Bn = \{0.1, 1.0, 10.0\}$.
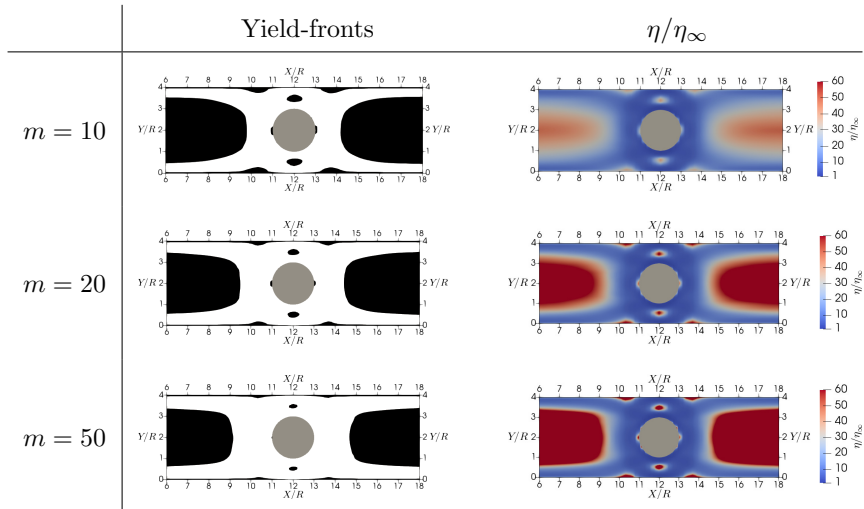
Figure 9: Viscoplastic SPH model; yield-fronts (left) and local viscosity (right) plots for the 2D flow around a cylinder with $L_x = 24$ and $Bn = 10.0$. From top to bottom $m = \{10, 20, 50\}$.

4. Thixo-viscoplastic models

Thixotropy is common in a wide range of complex fluids exhibiting a time-dependent response to applied stresses. When no stress is applied, at a microscopic level, a structured network (e.g. attractive particles or chains) is formed that can resist to applied stresses without flowing up to a certain threshold. When the applied forces become larger than a given threshold, the structured network starts to break down reducing the resistance of the fluid to flow. This micro-structure network requires time to build up and break down resulting in a thixotropic time scale that reflects in a transient rheology of these materials.

Following [64], it is possible to describe the micro-structural behaviour of these fluids introducing a micro-structure scalar parameter f defined in $[0:1]$: when $f = 1$ the micro-structure is defined as fully developed, while $f = 0$ means that the micro-structure has been completely destroyed.

In this paper, we use the micro-structure model described by Le-Cao et al. [15] to extend the viscoplastic Papanastasiou model described in Sec. 3 to include also thixotropic effects.

Following [15], the equation describing the time-evolution of the micro-structure parameter f is given by:

$$\dot{f} = a - (a + b\dot{\gamma})f, \tag{14}$$

where $\dot{f} = df/dt$ is the Lagrangian time-derivative of the structure parameter, while a and b are constants. In this case, a and $b\dot{\gamma}$ can be interpreted as the rate of build-up and break-down of the micro-structure network. In particular, the parameter a will play a special role when studying the rheology of these fluids, since $\lambda_0 = 1/a$ is associated to the characteristic thixotropic time scale. Introducing $\beta = b/a$, that is, the ratio between the build-up and break-down parameters, it is possible to rewrite Eq. (14) in the following way:

$$\dot{f} = \frac{1 - (1 + \beta\dot{\gamma})f}{\lambda_0}. \tag{15}$$

Eq. (15) can be integrated over time to obtain the following exact solution:

$$f = \frac{1}{1 + \beta\dot{\gamma}} \left(1 - e^{-\frac{(1+\beta\dot{\gamma})t}{\lambda_0}} \right) + f_0 e^{-\frac{(1+\beta\dot{\gamma})t}{\lambda_0}}, \tag{16}$$

where f_0 is the initial condition for f. It is noteworthy that if $\beta \rightarrow 0$, i.e. the build-up parameter is large compared to that of break-down ($a >> b$), then $f \rightarrow 1$ and the microstructure network tends to its highest level. Conversely, if $\beta \rightarrow \infty$, i.e. the build-up parameter is significantly smaller compared to that of break-down ($a << b$), then $f \rightarrow 0$ and the microstructure network is completely destroyed.

Eq. (15) admits also a solution at equilibrium for $t \rightarrow \infty$ given by:

$$f_e = \frac{1}{1 + \beta\dot{\gamma}}. \tag{17}$$

Notably, from Eq. (17), if $\dot{\gamma} = 0$, then $f_e = 1$, meaning that, at equilibrium, if no shear-rate is applied to the fluid, the micro-structure network is at its highest level and the fluid is not flowing. On the other hand, if $\dot{\gamma} \rightarrow \infty$, then $f_e \rightarrow 0$, meaning that the micro-structure network is completely destroyed.

Eq. (4) for viscoplastic fluids can be modified to include thixotropy in the following way:

$$\begin{cases} \eta = \eta_\infty(1 + \alpha f) + \dfrac{f\tau_y}{\dot{\gamma}} \left(1 - e^{-m\dot{\gamma}}\right), \\[2mm] \boldsymbol{\tau} = \left[\eta_\infty(1 + \alpha f) + \dfrac{f\tau_y}{\dot{\gamma}} \left(1 - e^{-m\dot{\gamma}}\right)\right] \dot{\boldsymbol{\gamma}}, \end{cases} \tag{18}$$

where α is a constitutive constant.

The extreme responses of this new thixo-viscoplastic model are, on the one hand, when $f = f_e = 1$, i.e. for $\dot{\gamma} \rightarrow 0$, the viscosity displayed in Eq. (18) reaches its maximum value equal to:

$$\eta = \eta_\infty(1 + \alpha) + m\tau_y.$$

On the other hand, when $f = f_e = 0$, i.e. when $\dot{\gamma} \rightarrow \infty$, the viscosity reduces to $\eta = \eta_\infty$ reflecting a material with a Newtonian fluid viscosity equal to $\eta = \eta_\infty$.

It is possible to define a criterion to track the yielded/unyielded regions also for a thixo-viscoplastic fluid by modifying the criterion given in Eq. (8) and taking into account the structure parameter f, as follows:

$$\begin{cases} yielded: & \tau > f\tau_y, \\ un-yielded: & \tau \leq f\tau_y. \end{cases} \tag{19}$$

19

4.1. Model validation: simple shear

A first group of SPH simulations have been performed to test the thixo-viscoplastic model rheology. As in the case of the viscoplastic Papanastasiou model in Sec. 3.1.1, the fluid domain is a square box of size $L = 10$ and, in order to impose a uniform shear flow, two rigid plates are considered in the planes normal to the y-direction, moving in opposite directions along the x-axis. Periodic boundary conditions have been set in the x-direction. For all the solutions presented in this section, the SPH resolution used is $L/\Delta r = 50$, where Δr is the mean particle spacing. The total number of SPH particles in this case is $N_{SPH} = 2500$. The fluid viscosity and density are $\eta_\infty = 15$ and $\rho = 1.0$, respectively, while the structure-parameter initial condition is imposed at $f_0 = 1$, which implies a fully structured material at the start of the simulation. The overall fluid viscosity and shear-stress are calculated with Eq. (12) directly from the time-averaged tangential force acting on the walls.

In order to minimize fluid inertial effects and to be able to accurately capture the transient behaviour of the thixo-viscoplastic model, the parameters a and b of Eq. (14) must be chosen such that $\lambda_0 > L^2/\nu$, where $\nu = \eta_\infty/\rho$. For this reason, we choose $\lambda_0\nu/L^2 = 6$ and $\beta = 1$.

A first set of simulations have been performed taking $\tau_y = 0$ and varying the constitutive parameter $\alpha = \{1, 2, 4\}$. Steady-state solutions in the form of non-dimensional viscosity and shear-stress are shown in Fig. 10, while Fig. 11 shows the viscosity transient evolution for two values of $\dot{\gamma} = \{0.1, 0.9\}$ and $\alpha = 1$.

In the transient case, time has been made non dimensional as $t' = t\nu/L^2$, where L is the fluid-domain height. Solutions are compared against the theoretical values obtained from Eq. (16), Eq. (17) and Eq. (18). This comparison shows a good agreement between simulations and theory for both the steady and transient shear viscosity and shear-stress.

A second set of simulations for a thixo-viscoplastic fluid have been performed using $\alpha = 1.0$ and yield stress $\tau_y = 10$, while varying $m = \{10, 20, 50\}$. Solutions for the steady viscosity and shear stress are shown in Fig. 12, while Fig. 13 shows the transient η and τ response under $\dot{\gamma} = \{0.0005, 0.009, 0.1, 0.3, 0.9\}$ and
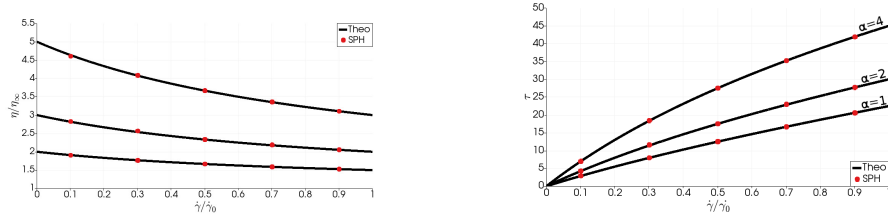
20

Figure 10: Thixo-viscoplastic SPH model. Steady shear viscosity (left) and shear stress (right) as a function $\dot{\gamma}$. Simulations were performed using three different values of $\alpha = \{1, 2, 4\}$ and fixing $\eta_\infty = 15.0$, $\rho = 1.0$ and $\tau_y = 0.0$. Results are compared with the theoretical values given by Eq. (18) and Eq. (17) .
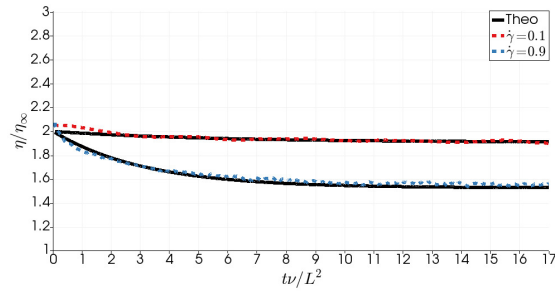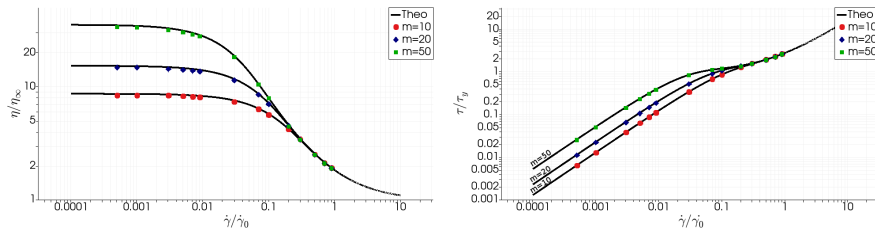

Figure 11: Thixo-viscoplastic SPH model. Viscosity transient-evolution for two different values of $\dot{\gamma} = \{0.1, 0.9\}$ and $\alpha = 1$. Simulations were performed fixing $\eta_\infty = 15.0$, $\rho = 1.0$ and $\tau_y = 0.0$. Results are compared with the theoretical values given by Eq. (16) and Eq. (18)..

$m = 10$. These numerical solutions agree with those provided by theory in

Figure 12: Thixo-viscoplastic SPH model. Steady viscosity (left) and shear stress (right) as a function $\dot{\gamma}$. Simulations were performed using three different values of $m = \{10, 20, 50\}$ and fixing $\eta_\infty = 15.0$, $\rho = 1.0$, $\alpha = 1.0$ and $\tau_y = 10.0$. Results are compared against theoretical values given by Eq. (17) and Eq. (18).
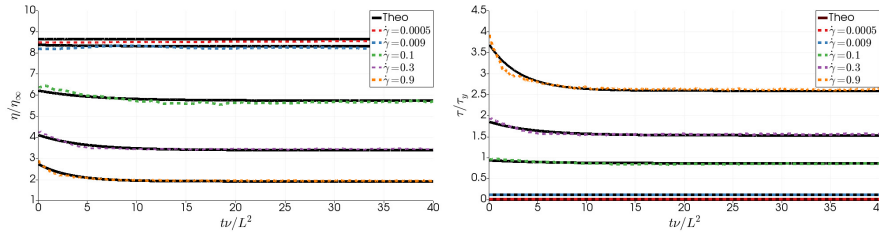
310

21

Figure 13: Thixo-viscoplastic SPH model. Viscosity (left) and shear stress (right) transient evolution for five different values of $\dot{\gamma} = \{0.0005, 0.009, 0.1, 0.3, 0.9\}$ and $m = 1$. Simulations were performed fixing $\eta_\infty = 15.0$, $\rho = 1.0$ and $\tau_y = 10.0$. Results are compared with the theoretical values given by Eq. (16) and Eq. (18) .

Eq. (16) and Eq. (18). It is important to note that all these simulations started with a fully developed fluid microstructure ($f_0 = 1$) in order to test the ability to correctly capture the microstructure destruction.

In order to further examine the ability of the thixo-viscoplastic SPH model to resolve the transient response given by theory, a third set of simulations has been performed. In Fig. 14, transient solutions are provided in terms of viscosity and shear-stress against step-changes of shear-rate, for which the microstructure dynamics (structure build-up and break-down) is recorded. The simulation protocol under shear-rate imposition (depicted at the bottom of Fig. 14) for these transient solutions is: the calculation starts under a reference shear-rate of $\dot{\gamma} = 0.1$ and, after reaching the corresponding steady-state, the shear-rate is suddenly to $\dot{\gamma} = 0.9$. After reaching the new steady-state, the shear-rate is switched back to the reference value of $\dot{\gamma} = 0.1$. Then, after steady-state attainment, a decrease of shear-rate towards $\dot{\gamma} = 0.01$ is imposed, followed by a last step back to the reference shear-rate value. As it is apparent in Fig. 14, numerical solutions obtained with our thixo-viscoplastic SPH model concur with those obtained theoretically using Eq. (18), where dimensionless viscosity and shear-stress display transient phases as a response to the shear-rate step-changes. Bottom plots of Fig. 14 shows the different shear rates used for this set of simulations.

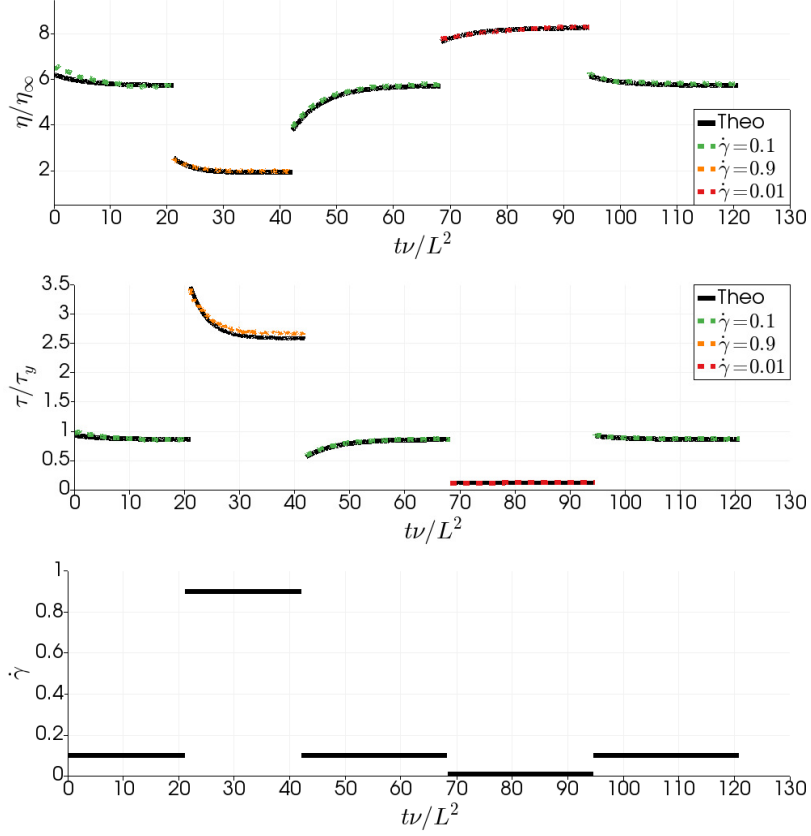Finally a convergence test have been performed using the case reported in

22

Figure 14: Thixo-viscoplastic SPH model. Viscosity (top) and shear stress (center) transient evolution changing the shear rate. The simulation protocol under shear-rate imposition, depicted in the bottom plot, for these transient solutions is: (i) the calculation starts under a reference shear-rate of $\dot{\gamma} = 0.1$, (ii) after reaching the corresponding steady-state, the shear-rate is suddenly to $\dot{\gamma} = 0.9$. (iii) After reaching the new steady-state, the shear-rate is switched back to the reference value of $\dot{\gamma} = 0.1$. This process is then repeated lowering the shear-rate to $\dot{\gamma} = 0.01$.

Fig. 14: transient solutions are provided in terms of viscosity against step-changes of shear-rate using three different resolutions $L/\Delta x = 25, 50, 100$. Obtained results are shown in Fig. 15 where the viscosity transient evolution is compared with the exact solution given by Eq. (18). The error with respect to
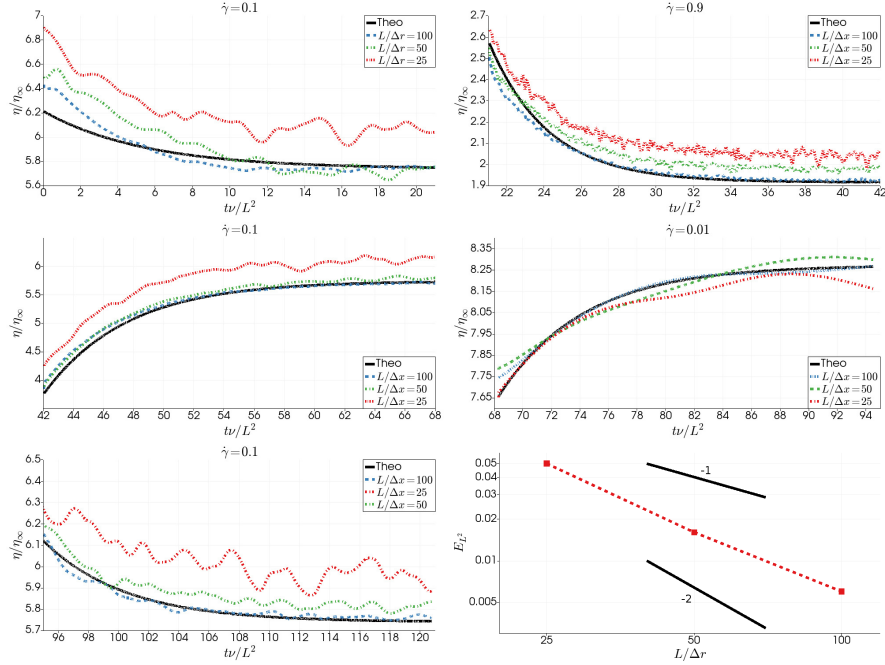
Figure 15: Thixo-viscoplastic SPH model. Convergence study using three different resolutions $L/\Delta x = 25, 50, 100$ for the case of Fig. 14. The results obtained for the viscosity transient evolution is compared with the exact solution given by Eq. (18). Bottom right plot depicts the error, evaluated using Eq. (20) with respect to the analytical solution, as a function of the resolution. In this case the Order of convergence is between 1 and 2.

the theoretical solution have been evaluated using and L^2 norm

$$E_{L^2} = \left(\frac{\int |\eta_{SPH}(t) - \eta_{theo}(t)|^2 dt}{\int |\eta_{theo}(t)|^2 dt} \right)^{1/2} \tag{20}$$

where η_{SPH} is the viscosity evaluated from the simulation and η_{theo} is the one given by Eq. (18).

Bottom right plot of Fig. 15 shows the errors evaluated using Eq. (20) as a function of the resolution. The order of convergence is between 1 and 2, as expected with SPH when analysing on quantities involving the velocity derivatives or their combinations as shown in [65] and [66].

24

4.2. 2D flow around a cylinder

In this section, the 2D flow around a circular cylinder of a thixo-viscoplastic fluid described by Eq. (18) is investigated. In order to correctly analyse and describe the physics of these flows, another non-dimensional quantity will be used, the Thixotropy number Th, defined as [4]:

$$Th = \frac{b}{a}\dot{\gamma}^* = \frac{bU_0}{aR}. \qquad (21)$$

where $\dot{\gamma}^* = \frac{U_0}{R}$ is the characteristic shear rate of the problem. For Th close to zero, f relaxes quickly to 1 and a pure viscoplastic Papanastasiou model is recovered, while $Th >> 1$ means that the microstructure network is completely destroyed.

Simulations are performed using three different Bingham numbers $Bn = \{0.1, 1.0, 10.0\}$. For each Bn, thixotropy is considered with three different Th-levels under $Th = \{0.5, 1.0, 2.0\}$ while keeping $\lambda_0 = 4$ constant. In Fig. 16-Fig. 19, steady-state solutions are analysed in terms field-plots of time-averaged yield-fronts, local viscosity, structure parameter and streamlines, and they are compared, whenever possible, to the results obtained with the Papanastasiou viscoplastic model described in Sec. 3. The same computational setup used for the simulations presented in Sec. 3 and represented in Fig. 3 has been used with $L_x = 24$, $\eta_\infty = 15$ and $U_0 = 1$.

In Fig. 16, yield-fronts reveal a complex phenomenology with the change of Bn and Th.

Under fixed Th=0 (viscoplastic solutions), the growth of slender un-yielded regions are recorded with origin on the channel centre that widen with Bn-increase. In the extreme case of $Bn=10$, the solidified material nearly covers the whole channel cross-section away from the obstacle, with yielded fluid moving between the solid-like material and the channel walls. The boundary of the un-yielded material patches take a rounded shape when approaching the obstacle and the growth of isolated islands with base on the poles of the cylinder is registered alongside triangular solid-like patches attached to the walls.

25

Inclusion of thixotropy through Th-increase brings asymmetry to this phenomenology. Here, in contrast to the viscoplastic $Th = 0$-case, the thixo-viscoplastic $Th = 2$ solution appears with asymmetric yield-fronts with respect to the cylinder axis; i.e. the un-yielded region upstream of the cylinder blocks the channel with a wider and more blunt solid-profile than that downstream of the obstacle. In addition, the triangular solid-like patches on the channel walls and the islands located on the cylinder poles appear smaller. These changes in yield-fronts may be correlated with the structure-dependent response of the thixo-viscoplastic fluid, for which viscosity and yield-stress contributions hold an explicit functionality with the structure parameter, as specified in Eq. (18).

Such findings are supported by the structure-parameter and viscosity plots in Fig. 17 and Fig. 18, respectively, where a one-to-one correspondence on location and strength in the structure and yield-front display is recorded. Here, at fixed thixo-viscoplastic $Th = 2$ level, Bn-increase provokes the growth of red zones of relatively high structure-parameter and viscosity values; these progressively cover the channel cross-section with Bn-rise, leaving thin gaps of un-structured low-viscosity material near the channel walls at $Bn = 10$. This is accompanied by blue zones near the cylinder surface that indicate the presence of fluidised material in those shear-dominated regions; this blue regions elongate behind the obstacle, creating a tail-like feature, more prominent with Bn-rise. The un-yielded front behind the cylinder appears weaker and somewhat smaller compared to that upstream.

In Fig. 19 streamline patterns are plotted for the same Th-Bn domain. Here, conspicuously, the asymmetry recorded is yield-fronts, structure-parameter and viscosity is absent in the flow kinematics. Nevertheless, it is noteworthy the increase of flow-rate apparent on $Bn = 10$ solutions, with stronger red streamlines passing around the cylinder for all Th instances.
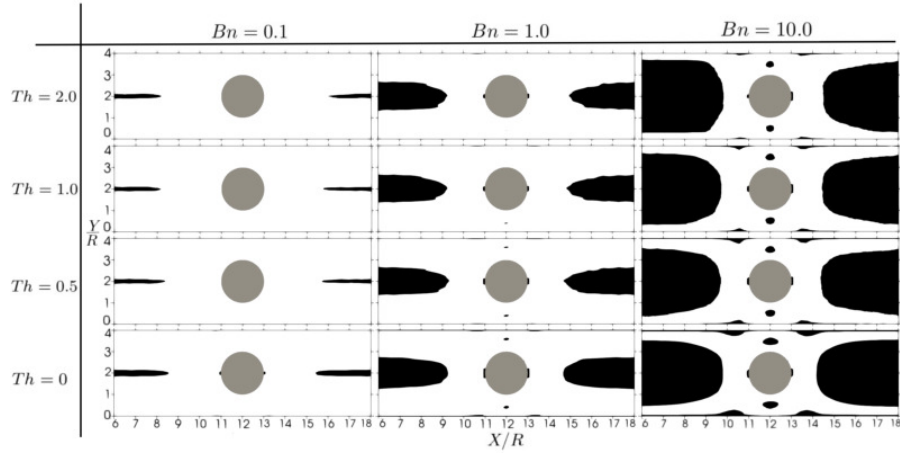
26

Figure 16: Comparison of yield-fronts using different value of Th and Bn: from top to bottom $Th = \{2.0, 1.0, 0.5\}$, from left to right $Bn = \{0.1, 1.0, 10.0\}$. The pure viscoplastic case has been reported in last row for comparison.
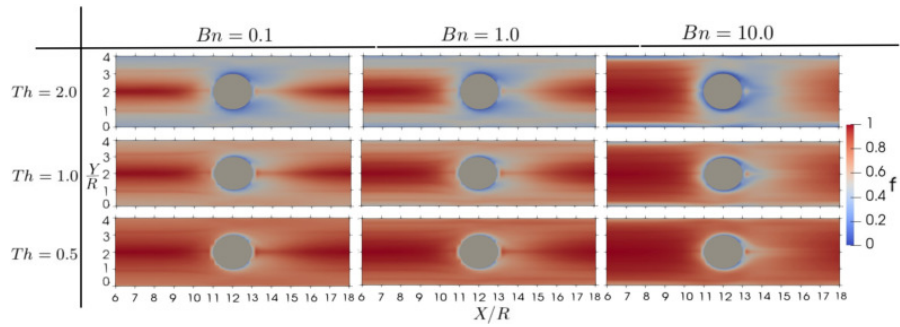

Figure 17: Comparison of structure-parameter fields using different values of Th and Bn: from top to bottom $Th = \{2.0, 1.0, 0.5\}$, from left to right $Bn = \{0.1, 1.0, 10.0\}$.
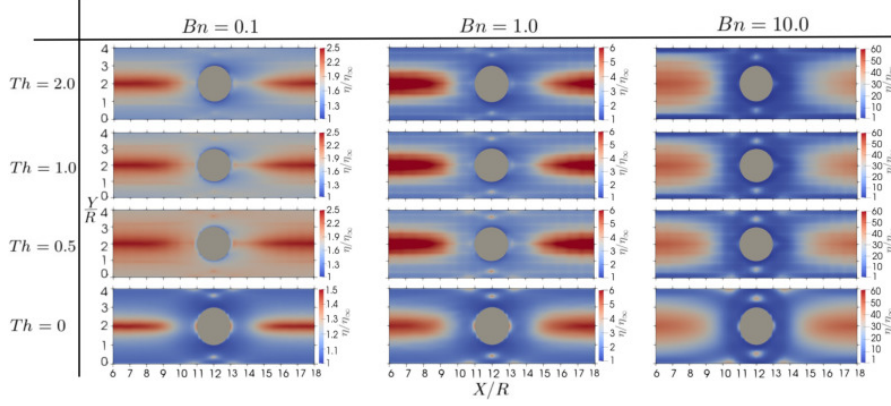
Figure 18: Comparison of viscosity fields using different value of Th and Bn: from top to bottom $Th = \{2.0, 1.0, 0.5\}$, from left to right $Bn = \{0.1, 1.0, 10.0\}$.
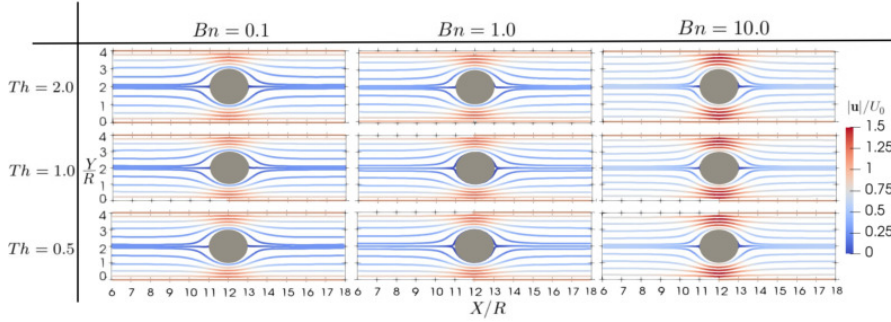

Figure 19: Comparison of streamlines using different value of Th and Bn: from top to bottom $Th = \{2.0, 1.0, 0.5\}$, from left to right $Bn = \{0.1, 1.0, 10.0\}$.

5. Conclusions

In this work the 2D viscoplastic and thixo-viscoplastic flow around a cylinder is simulated using an SPH method. The most important novelty introduced in this paper is the use of an SPH method to simulate these kind of flows and in particular on a rigorous validation of the fluid-structure interaction in terms of yielded and un-yielded regions for the viscoplastic flow around a cylinder and effect of thixotropy. The Bingham viscoplastic model with the Papanastasiou regularization was introduced in the SPH method to simulate apparent yield

28

stress fluids. The validation was performed in two set of simulations. A first set was considered to test the fluid rheology under viscometric conditions keeping the yield stress constant while varying the applied shear-rate. The obtained results have been successfully compared with the theoretical ones. A second set of numerical experiments was performed to test the SPH ability to reproduce the interaction of a viscoplastic fluid with a cylinder in terms of yielded and un-yielded regions. In this case, tests were performed varying the Bingham number and obtained SPH results compared to the ones of a FVM (i.e. RheoTool) solver with a good level of agreement.

To describe thixotropic behaviour, a microstructural parameter was introduced which determines the amount of network developed within a Lagrangian element. The dynamics of this parameter follows a shear-dependent construction and relaxation dynamics. A first set of simulations was performed to test the fluid rheology keeping the yield stress and the thixotropy micro-structure parameters constant while varying the applied shear-rate. The obtained results have been successfully compared with the theoretical ones. A second set of simulations was performed to investigate the interaction of a thixo-viscoplastic fluid with a cylinder. In this case, a Thixotropy number was introduced, which is defined as the ratio between the micro-structure build-up and break down time-scales. Simulations were performed by varying the Bingham as well as the Thixotropy numbers over a wide regime. Obtained results showed that thixotropy generates an asymmetry within the fluid flow around a cylinder, particularly evident for high Bingham and Thixotropy numbers.

The current validated thixo-viscoplastic SPH model will be used in the future to explore the rheology of complex thixotropic particle suspensions, following the work done in [67] with viscoelastic matrices.

Acknowledgements

29

References

References

[1] Mewis J. Thixotropy - a general review. J Non-Newton Fluid Mech. 1979;6:1–20.

[2] Barnes HA. Thixotropy - a review. J Non-Newton Fluid Mech. 1997;70:1–33.

[3] Mewis J, Wagner NJ. Thixotropy. Adv Colloid Interf Sci. 2009;147-148:214–227.

[4] Larson RG, Wei Y. A review of thixotropy and its rheological modeling. J Rheol. 2019;63:477–501.

[5] Barnes HA, Walters K. The yield stress myth? Rheol Acta. 1985;24:323–326.

[6] Barnes HA. The yield stress - a review or '$\pi\alpha\nu\tau\alpha$ $\rho\epsilon\iota$' - everything flows? J Non-Newton Fluid Mech. 1999;81:133–178.

[7] Moller PCF, Mewis J, Bonn D. Yield stress and thixotropy: on the difficulty of measuring yield stresses in practice. Soft Matter. 2006;2:274–283.

[8] Barnes HA. The 'yield stress myth?' paper - 21 years on. Appl Rheol. 2007;17:43110 1–5.

[9] Mitsoulis E. Flows of viscoplastic materials: models and computations. Rheol Rev. 2007;1:135–178.

[10] Malkin A, Kulichikhin V, Ilyin S. A modern look on yield stress fluids. Rheol Acta. 2017;56:177–188.

[11] Coussot P. Yield stress fluid flows: A review of experimental data. J Non-Newton Fluid Mech. 2014;211:31–49.

[12] Larson RG. Constitutive equations for thixotropic fluids. J Rheol. 2015;59:595–611.

[13] Mujumdar A, Beris AN, Metzner AB. Transient phenomena in thixotropic systems. J Non-Newton Fluid Mech. 2002;102:157–178.

[14] Fredrickson AG. A model for the thixotropy of suspensions. AIChE J. 1970;16:436–441.

[15] Le-Cao K, Phan-Thien N, Mai-Duy N, Ooi SK, Lee AC, Khoo BC. A microstructure model for viscoelastic–thixotropic fluids. Phys Fluids. 2020;32(12):123106.

[16] Syrakos A, Georgiou GC, Alexandrou AN. Thixotropic flow past a cylinder. J Non-Newton Fluid Mech. 2015;220:44–56.

[17] Mahmood R, Kousar N, Usman K, Mehmood A. Finite element simulations for stationary Bingham fluid flow past a circular cylinder. J Braz Soc Mech Sci Eng. 2018;40:459 1–9.

[18] Bui CM, Ho TX. Numerical study of an unsteady flow of thixotropic liquids past a cylinder. AIP Adv. 2019;9:115002 1–10.

[19] Bui CM, Ho TX. Flow of a Thixotropic Bingham Fluid over a Cylinder in Stationary and Non-Stationary Regimes. J Appl Fluid Mech. 2020;13:1527–1538.

[20] Bui CM, Ho TX. Influence of thixotropic parameters on a non-Newtonian fluid flow. AIP Adv. 2020;10:035303 1–9.

[21] Ellero M, Kröger M, Hess S. Viscoelastic flows studied by smoothed particle dynamics. J Non-Newton Fluid Mech. 2002;105(1):35–51.

[22] Ellero M, Tanner R. SPH simulations of transient viscoelastic flows at low Reynolds number. Journal of Non-Newtonian Fluid Mechanics. 2005;132(1-3):61–72.

[23] Rodriguez-Paz MX, Bonet J. A corrected smooth particle hydrodynamics method for the simulation of debris flows. Numer Methods Partial Differ Equ. 2004;20(1):140–163.

[24] Khanpour M, Zarrati AR, Kolahdoozan M, Shakibaeinia A, Amirshahi SM. Mesh-free SPH modeling of sediment scouring and flushing. Comput Fluids. 2016;129:67–78.

[25] Zhu H, Martys NS, Ferraris C, De Kee D. A numerical study of the flow of Bingham-like fluids in two-dimensional vane and cylinder rheometers using a smoothed particle hydrodynamics (SPH) based method. J Non-Newton Fluid Mech. 2010;165(7-8):362–375.

[26] Ghaïtanellis A, Violeau D, Ferrand M, Abderrezzak KEK, Leroy A, Joly A. A SPH elastic-viscoplastic model for granular flows and bed-load transport. Advances in Water Resources. 2018;111:156–173.

[27] Tran-Duc T, Ho T, Thamwattana N. A smoothed particle hydrodynamics study on effect of coarse aggregate on self-compacting concrete flows. International Journal of Mechanical Sciences. 2021;190:106046.

[28] Minatti L, Paris E. A SPH model for the simulation of free surface granular flows in a dense regime. Applied Mathematical Modelling. 2015;39(1):363–382.

[29] Fourtakas G, Rogers BD. Modelling multi-phase liquid-sediment scour and resuspension induced by rapid flows using Smoothed Particle Hydrodynamics (SPH) accelerated with a Graphics Processing Unit (GPU). Adv Water Resour. 2016;92:186–199.

[30] Nodoushan EJ, Shakibaeinia A. Multiphase mesh-free particle modeling of local sediment scouring with μ (I) rheology. J Hydroinformatics. 2019;21(2):279–294.

[31] Nabian MA, Farhadi L. Multiphase mesh-free particle method for simulating granular flows and sediment transport. J Hydraul Eng. 2017;143(4):04016102.

[32] Zhu C, Huang Y, Zhan LT. SPH-based simulation of flow process of a landslide at Hongao landfill in China. Nat Hazards. 2018;93(3):1113–1126.

[33] Paiva A, Petronetto F, Lewiner T, Tavares G. Particle-based viscoplastic fluid/solid simulation. Comput Aided Des. 2009;41(4):306–314.

[34] Xenakis AM, Lind SJ, Stansby PK, Rogers BD. An incompressible SPH scheme with improved pressure predictions for free-surface generalised Newtonian flows. J Non-Newton Fluid Mech. 2015;218:1–15.

[35] Martys NS, George WL, Chun BW, Lootens D. A smoothed particle hydrodynamics-based fluid model with a spatially dependent viscosity: application to flow of a suspension with a non-Newtonian fluid matrix. Rheol acta. 2010;49(10):1059–1069.

[36] Mitsoulis E. On creeping drag flow of a viscoplastic fluid past a circular cylinder: wall effects. Chem Eng Sci. 2004;59(4):789–800.

[37] Tokpavi DL, Magnin A, Jay P. Very slow flow of Bingham viscoplastic fluid around a circular cylinder. J Non-Newton Fluid Mech. 2008;154(1):65–76.

[38] Vahabi M. The effect of thixotropy on dam-break flow: a numerical study by smoothed particle hydrodynamics. J Braz Soc Mech Sci Eng. 2021;43(11):1–7.

33

[39] Sadeghy K, Vahabi M. The effect of thixotropy on a rising gas bubble: A numerical study. Korea Aust Rheol J. 2016;28(3):207–216.

[40] Español P, Revenga M. Smoothed dissipative particle dynamics. Phys Rev E. 2003;67(2):026705.

[41] Morris JP, Fox PJ, Zhu Y. Modeling low Reynolds number incompressible flows using SPH. J Comput Phys. 1997;136(1):214–226.

[42] Ellero M, Adams NA. SPH simulations of flow around a periodic array of cylinders confined in a channel. Int J Numer Methods Eng. 2011;86(8):1027–1040.

[43] Monaghan JJ. Simulating free surface flows with SPH. J Comput Phys. 1994;110(2):399–406.

[44] Bian X, Litvinov S, Qian R, Ellero M, Adams NA. Multiscale modeling of particle in suspension with smoothed dissipative particle dynamics. Phys Fluids. 2012;24(1):012002.

[45] Balmforth NJ, Frigaard IA, Ovarlez G. Yielding to stress: recent developments in viscoplastic fluid mechanics. Annu Rev Fluid Mech. 2014;46:121–146.

[46] Bingham EC. Fluidity and plasticity. vol. 2. McGraw-Hill; 1922.

[47] Herschel WH, Bulkley R. Konsistenzmessungen von gummibenzollösungen. Kolloid-Zeitschrift. 1926;39(4):291–300.

[48] Casson N. A flow equation for pigment-oil suspensions of the printing ink type. Rheology of Disperse Systems. 1959;.

[49] Bercovier M, Engelman M. A finite-element method for incompressible non-Newtonian flows. J Comp Phys. 1980;36(3):313–326.

[50] Trémolières R, Lions JL, Glowinski R. Numerical analysis of variational inequalities. Elsevier; 2011.

[51] Papanastasiou TC. Flows of materials with yield. J Rheol. 1987;31(5):385–404.

[52] Mises Rv. Mechanik der festen Körper im plastisch-deformablen Zustand. Nachrichten von der Gesellschaft der Wissenschaften zu Göttingen, Mathematisch-Physikalische Klasse. 1913;1913(4):582–592.

[53] Thompson RL, Sica LUR, de Souza Mendes PR. The yield stress tensor. J Non-Newton Fluid Mech. 2018;261:211–219.

[54] Favero JL, Secchi AR, Cardozo NSM, Jasak H. Viscoelastic flow analysis using the software OpenFOAM and differential constitutive equations. J Non-Newton Fluid Mech. 2010;165(23-24):1625–1636.

[55] Habla F, Woitalka A, Neuner S, Hinrichsen O. Development of a methodology for numerical simulation of non-isothermal viscoelastic fluid flows with application to axisymmetric 4: 1 contraction flows. Chem Eng J. 2012;207:772–784.

[56] Holmes L, Favero J, Osswald T. Numerical simulation of three-dimensional viscoelastic planar contraction flow using the software OpenFOAM. Comput Chem Eng. 2012;37:64–73.

[57] Habla F, Obermeier A, Hinrichsen O. Semi-implicit stress formulation for viscoelastic models: Application to three-dimensional contraction flows. J Non-Newton Fluid Mech. 2013;199:70–79.

[58] Fernandes C, Araujo MSB, Ferrás LL, Nóbrega JM. Improved both sides diffusion (iBSD): A new and straightforward stabilization approach for viscoelastic fluid flows. J Non-Newton Fluid Mech. 2017;249:63–78.

[59] Liu J, Anderson KL, Sridhar N. Direct simulation of polymer fused deposition modeling (fdm)—an implementation of the multi-phase viscoelastic solver in OpenFOAM. Int J Comput Methods. 2020;17(01):1844002.

[60] Favero JL, Secchi AR, Cardozo NSM, Jasak H. Viscoelastic fluid analysis in internal and in free surface flows using the software OpenFOAM. Comput Chem Eng. 2010;34(12):1984–1993.

[61] Habla F, Tan MW, Haßlberger J, Hinrichsen O. Numerical simulation of the viscoelastic flow in a three-dimensional lid-driven cavity using the log-conformation reformulation in OpenFOAM®. J Non-Newton Fluid Mech. 2014;212:47–62.

[62] Pimenta F, Alves MA. rheoTool; 2016. `https://github.com/fppimenta/rheoTool`.

[63] Fattal R, Kupferman R. Constitutive laws for the matrix-logarithm of the conformation tensor. J Non-Newton Fluid Mech. 2004;123(2-3):281–285.

[64] Larson RG. The structure and rheology of complex fluids. vol. 150;.

[65] Rossi E, Colagrossi A, Graziani G. Numerical simulation of 2D-vorticity dynamics using particle methods. Computers & Mathematics with Applications. 2015;69(12):1484–1503.

[66] Colagrossi A, Rossi E, Marrone S. The Discrete Vortex Hydrodynamics method: similarities and differences with the SPH. In: 10th international SPHERIC workshop; 2015. p. 16–18.

[67] Vázquez-Quesada A, Español P, Tanner RI, Ellero M. Shear thickening of a non-colloidal suspension with a viscoelastic matrix. Journal of Fluid Mechanics. 2019;880:1070–1094.